

Dynamic Pressure Drag on Rising Buoyant Thermals in a Neutrally Stable Environment

HUGH MORRISON,^a NADIR JEEVANJEE,^b AND JUN-ICHI YANO^c

^a National Center for Atmospheric Research, Boulder, Colorado

^b Geophysical Fluid Dynamics Laboratory, Princeton, New Jersey

^c CNRM, UMR3589 (CNRS), Météo-France, Toulouse, France

(Manuscript received 12 October 2021, in final form 28 June 2022)

ABSTRACT: This study examines dynamic pressure drag on rising dry buoyant thermals. A theoretical expression for drag coefficient C_d as a function of several other nondimensional parameters governing thermal dynamics is derived based on combining the thermal momentum budget with the similarity theory of Scorer. Using values for these nondimensional parameters from previous studies, the theory suggests drag on thermals is small relative to that on solid spheres in laminar or turbulent flow. Two sets of numerical simulations of thermals in an unstratified, neutrally stable environment using an LES configuration of the Cloud Model 1 (CM1) are analyzed. One set has a relatively low effective Reynolds number R_e and the other has an order-of-magnitude-higher R_e ; these produce laminar and turbulent resolved-scale flows, respectively. Consistent with the theoretical C_d , the magnitude of drag is small in all simulations. However, whereas the laminar thermals have $C_d \approx 0.01$, the turbulent thermals have weakly *negative* drag ($C_d \approx -0.1$). This difference is explained by the laminar thermals having near vertical symmetry but the turbulent thermals exhibiting considerable vertical asymmetry of their azimuthally averaged flows. In the laminar thermals, buoyancy rapidly becomes concentrated around the main centers of rotation located along the horizontal central axis, leading to expansion of thermals via baroclinic vorticity generation but doing little to break vertical symmetry of the flow. Vertical asymmetry of the azimuthally averaged flow of turbulent thermals is attributed mainly to small-scale resolved eddies that are concentrated in the upper part of the thermals.

KEYWORDS: Buoyancy; Eddies; Pressure; Turbulence; Large eddy simulations

1. Introduction

Thermals are a common feature of many buoyancy-driven flows, including dry and moist convection in the atmosphere (e.g., Turner 1973; Yano 2014). They consist of a quasi-spherical region of rising fluid that is buoyant relative to the surrounding fluid. Dimensional analysis can be applied to understand basic flow features of thermals assuming that their shape is self-similar—that is, it is geometrically similar over time (e.g., Scorer 1957). Considerable progress has been made in understanding dry thermal dynamics in the past several decades using laboratory observations (Scorer 1957; Turner 1957; Woodward 1959; Richards 1961; Sánchez et al. 1989; Johari 1992; Bond and Johari 2005, 2010; Zhao et al. 2013) and numerical models (Lilly 1962; Ogura 1962; Lundgren et al. 1992; Li and Zhang 1996; Ma and Li 2001; Li and Ma 2003; Lai et al. 2015; Lecoanet and Jeevanjee 2019, hereafter LJ2019; McKim et al. 2020). Many of these studies focused on the spreading rate of thermals as they rise and entrain surrounding fluid (Scorer 1957; Richards 1961; Lai et al. 2015; LJ2019). This effort has included studying the relation between a thermal’s impulse and its circulation which is closely related to its spreading rate (Turner 1957; Lai et al. 2015; McKim et al. 2020). These studies have generally confirmed results from dimensional analysis and similarity theory. Key characteristics (after spinup) are that the thermal radius R depends linearly on height z (i.e., dR/dz is a constant), the Froude number and circulation are constant over time, and

thermal velocity w scales inversely with the square root of time t ($w \propto t^{-1/2}$) (e.g., McKim et al. 2020).

A resurgence of work on thermal dynamics in the atmospheric sciences community has been motivated by recent observational and high-resolution modeling studies showing that thermals are practically ubiquitous in moist convection (Zhao and Austin 2005; Blyth et al. 2005; Damiani et al. 2006; Heus et al. 2009; Sherwood et al. 2013; Romps and Charn 2015). This work has focused on the entrainment behavior and spreading rates of moist thermals¹ within convective clouds (Romps and Charn 2015; Hernandez-Deckers and Sherwood 2016, 2018) and understanding differences between spreading rates of dry and moist thermals (Vybhav and Ravichandran 2022; Morrison et al. 2021, hereafter MPS2021). Another aspect receiving recent attention is the drag force on moist thermals as they rise (Sherwood et al. 2013; Romps and Öktem 2015; Romps and Charn 2015; Hernandez-Deckers and Sherwood 2016; Morrison and Peters 2018). Relatedly, a “drag” term is often incorporated into the vertical momentum equation in convection parameterization schemes (e.g., Donner 1993; Siebesma et al. 2003; Bretherton et al. 2004). However, such schemes generally use the vertical momentum equation for steady state plumes, and the physical meaning of dynamic drag in this context is not clear in contrast to an ascending thermal or starting plume (an ascending plume with a thermal-like head).

Corresponding author: Hugh Morrison, morrison@ucar.edu

¹ Hereafter “moist thermals” will specifically refer to thermals associated with clouds undergoing phase changes in water.

In past literature on thermal drag, as well as the current paper, the drag coefficient C_d is derived using the drag law:

$$F_d = C_d \rho w_{\text{th}}^2 A / (2V), \quad (1)$$

where F_d is the drag force per unit volume of the thermal, ρ is the fluid density, w_{th} is the thermal's ascent rate, A is its horizontal cross sectional area, and V is the thermal's volume. This follows from the standard drag law divided by V to give a drag force per unit volume. Based on large-eddy simulation (LES) of deep convective clouds, Sherwood et al. (2013) proposed that cloud thermals experience little drag and thus have $C_d \approx 0$ —that they are “slippery.” The authors made an analogy to Hill's (nonbuoyant) analytic spherical vortex, which has a similar overall dynamical structure to their moist thermals and formally has zero drag. In contrast, Romps and Charn (2015) showed considerable pressure drag on cloud thermals in their LES of convective clouds—which they termed “sticky” thermals—with a mean drag coefficient $C_d \approx 0.6$. The “slippery” versus “sticky” thermal debate largely centered on differences in how the drag force F_d was defined. That is, the “drag law” given by (1) does not by itself define C_d because it depends on how F_d is determined; Sherwood et al. (2013) defined F_d as the drag from momentum entrainment, whereas Romps and Charn (2015) defined F_d as the thermal volume-integrated perturbation pressure gradient force (where the perturbation was relative to a hydrostatically balanced background state). Hernandez-Deckers and Sherwood (2016) also calculated drag from the perturbation pressure forcing on moist thermals in LES and found a dominant balance between perturbation pressure drag and buoyancy.

Note that Romps and Charn (2015) and Hernandez-Deckers and Sherwood (2016) calculated thermal drag using the *total* perturbation pressure gradient forcing. This forcing can be further divided into buoyant and dynamic components (p_B and p_D , respectively) based on terms in the diagnostic Poisson perturbation pressure equation (Markowski and Richardson 2011). The Laplacian of p_B depends on the vertical gradient of fluid buoyancy B , while the Laplacian of p_D depends on the flow field. Thus, the p_B forcing on a thermal depends on the magnitude and shape of the thermal's B field, and can be well understood from an analogy to magnetostatics (Tarshish et al. 2018). In short, the relative p_B force opposing the thermal's upward-directed B force depends on aspect ratio (width to height) of the thermal's region of buoyancy. Other studies have used simplified expressions to similarly show that the p_B forcing for moist convection depends approximately on a buoyant updraft's aspect ratio (Weisman et al. 1997; Pauluis and Garner 2006; Morrison 2016; Peters 2016). Given the close connection of p_B to the B field, several studies have discussed updraft acceleration in terms of an effective buoyancy equal to the sum of the B and p_B forcings (Davies-Jones 2003; Jeevanjee and Romps 2015, 2016; Peters 2016; Jeevanjee 2017).

While the p_B forcing on a thermal is relatively simple to conceptualize from the thermal's B field, drag arising from p_D forcing is inherently more challenging to understand. The p_D field itself can be split into rotational and divergence components (sometimes referred to as “spin” and “splat”), as well as

linear and nonlinear terms in the presence of environmental shear. These components must sum in a way such that the total p_D field is consistent with nondivergence of the fluid (for incompressible flow). Calculating dynamic pressure drag by the integral of $-\partial p_D / \partial z$ over the thermal's volume (where z is height)—or equivalently, $p_D \hat{\mathbf{n}} \cdot \hat{\mathbf{k}}$ integrated along the thermal's upper and lower boundaries following Gauss's theorem—nonzero p_D drag fundamentally must arise from a vertical asymmetry in p_D along the upper and lower boundaries of the thermal (where $\hat{\mathbf{n}}$ and $\hat{\mathbf{k}}$ are unit vectors normal to the thermal's surface and in the vertical, respectively). Given overall similarity of the flow structure of buoyant thermals to Hill's vortex (Sherwood et al. 2013; Zhao et al. 2013; Romps and Charn 2015), one might anticipate small p_D drag given that Hill's vortex has no drag; its p_D field is exactly vertically symmetric about the vortex center. However, in contrast to Hill's vortex, the buoyancy within thermals might in general be expected to drive vertical asymmetry of the flow and hence dynamic pressure drag. The key question is the magnitude and nature of this drag. Is it a significant component of the thermal's momentum budget, generally, or small relative to the other terms (B forcing, p_B forcing, momentum entrainment)?

Perhaps surprising in light of its relative simplicity, drag on rising dry thermals has received less attention than drag on moist thermals. Drag on nonbuoyant vortex rings was studied by Maxworthy (1974) and Gan et al. (2012), and drag on buoyant vortex ring *bubbles* was studied recently in Vassel-Be-Hagh et al. (2015). However, we are not aware of any study of the drag on buoyant thermals in which the underlying vortex ring is composed of the same fluid as the ambient, as is the case in atmospheric convection.

There may be some correspondence of drag on dry thermals to form drag on solid bodies in flow, since the latter also occurs via p_D gradient forcing in the direction of the mean flow. A well-known feature of drag around solid bodies in a viscous fluid is a Reynolds number dependence and, in particular, changes in C_d with a transition from laminar to turbulent flow. For instance, it is well-known that there is often a sharp decrease in C_d associated with the development of turbulence (referred to as “drag crisis”). This occurs because turbulent eddies impact vortex shedding and pressure recovery in the object's wake, thereby influencing drag. However, a critical distinction with drag on solid bodies is that thermals represent a region within a continuous fluid, and generally have an internal circulation and changes in size as they evolve and entrain the surrounding fluid. Thus, it is unclear how knowledge of form drag on solid bodies might translate to drag on thermals, whether in laminar or turbulent flow.

The purpose of this study is to examine in detail the dynamic pressure drag on rising buoyant thermals. Given the limited knowledge on thermal drag generally, we focus here on the simple case of dry buoyant thermals in an unstratified incompressible fluid. The more complicated problem of drag on moist thermals in a stratified environment is left to future work. Note that other types of drag, including wave drag or other drag-like forces (e.g., Kutta–Joukowski lift caused by rotating bodies in flow, commonly known as the “Magnus effect”), may impact both thermals and solid bodies in flow.

In this study we do not investigate these other forces and instead focus specifically on dynamic pressure drag on thermals in a neutrally stable background fluid with no shear (hence no wave drag or drag-like forces associated with shear). We first derive a theoretical expression for C_d based on the thermal’s vertical momentum budget combined with the similarity theory of [Scorer \(1957\)](#). We then obtain C_d directly from numerical simulations of rising thermals using a fully dynamical model that solves the incompressible Boussinesq equations of motion. Two sets of simulations are analyzed: one with a relatively low effective Reynolds number that produces laminar thermals with smooth resolved-scale flow, and the other with a higher effective Reynolds number leading to thermals with turbulent-like flow. It is found that dynamic pressure drag is relatively small (say, compared to flow around a solid sphere), but interestingly the turbulent thermals have a weakly negative drag in contrast to nearly zero drag for the laminar thermals.

The rest of the paper is organized as follows. [Section 2](#) gives an overview of the thermal momentum budget, the solution for thermal dynamics from similarity theory, and the theoretical analysis of C_d . The numerical model description is in [section 3](#). [Section 4](#) presents model results. A summary and conclusions are given in [section 5](#).

2. Theory

a. Thermal momentum budget

To understand and quantify dynamic pressure drag on thermals, we first present an equation for the thermal vertical momentum budget. Defining a thermal as occupying some portion of space Ω within the domain, we integrate the vertical momentum equation over Ω to obtain the momentum budget. Similar to previous methods for thermal identification and tracking (e.g., [Romps and Charn 2015](#); [LJ2019](#)), we define Ω as the region of space bounded by a closed streamline in the azimuthally averaged (around the thermal’s central vertical axis) flow that intersects with the thermal top. Defined in this way, the vertical velocity w averaged over Ω is nearly equal to the rate at which the thermal top ascends (see [section 3c](#) for details on the thermal tracking method applied to the numerical simulations here). Using Gauss’s theorem to relate the divergence of the momentum field over Ω to the flux of momentum across the surface of Ω , similar to [Romps and Charn \(2015\)](#), gives

$$\begin{aligned} \frac{d}{dt} \int_{\Omega(t)} \rho w d^3x &= - \int_{\Omega(t)} \frac{\partial p_B}{\partial z} d^3x - \int_{\Omega(t)} \frac{\partial p_D}{\partial z} d^3x \\ &+ \int_{\Omega(t)} \rho B d^3x + \int_{\partial\Omega(t)} (\hat{\mathbf{n}} \cdot \mathbf{u}_e) \rho w d^2x, \end{aligned} \quad (2)$$

where $\partial\Omega(t)$ is the two-dimensional boundary of $\Omega(t)$, and \mathbf{u}_e is an effective entrainment velocity defined as the displacement rate of the thermal boundary \mathbf{u}_b relative to flow velocity \mathbf{u} , i.e., $\mathbf{u}_e = \mathbf{u}_b - \mathbf{u}$. We have divided the pressure forcing into buoyant (p_B) and dynamic (p_D) pressure components.

Dividing by thermal volume V and rearranging terms, the thermal-averaged vertical momentum budget becomes

$$\rho \frac{dw_{\text{th}}}{dt} = -F_{pB} - F_{pD} + \rho B_{\text{th}} + E, \quad (3)$$

where $w_{\text{th}} \equiv V^{-1} \int_{\Omega(t)} w d^3x$ is the thermal-averaged w assumed to be equal to the thermal ascent rate, $F_{pD} \equiv V^{-1} \int_{\Omega(t)} (\partial p_D / \partial z) d^3x$ is the thermal-averaged dynamic pressure drag force, $F_{pB} \equiv V^{-1} \int_{\Omega(t)} (\partial p_B / \partial z) d^3x$ is the thermal-averaged buoyancy pressure force, $\dot{E} \equiv V^{-1} \int_{\partial\Omega(t)} (\hat{\mathbf{n}} \cdot \mathbf{u}_e) \rho w d^2x - V^{-1} (dV/dt) w_{\text{th}} \rho$ is the momentum entrainment, and $B_{\text{th}} \equiv V^{-1} \int_{\Omega(t)} B d^3x$ is the thermal-averaged buoyancy (hereafter in most instances we drop subscript “th” for the thermal-averaged B and w). For simplicity we have assumed Boussinesq incompressible flow so that ρ is constant. Our study focuses on dynamic pressure drag—the second term on the rhs of (3)—which closely accords with other notions of fluid dynamical drag. Thus, we obtain C_d using (1) with $F_d = F_{pD}$.

Note that E represents the import or export of vertical momentum to/from the thermal owing to a difference between the local flow speed normal to the thermal surface and the surface displacement rate. Physically, nonzero E can occur by changes in the thermal volume (e.g., expansion) or local inflow and outflow across the thermal surface, or a combination of the two. As shown by [LJ2019](#) and [McKim et al. \(2020\)](#), thermal expansion driven by baroclinic vorticity generation associated with the thermal’s buoyancy structure is the main process leading to $E < 0$; smaller scale mixing is relatively unimportant even in turbulent thermals ([LJ2019](#)). For simplicity and consistent with these previous studies we will refer to this baroclinically driven expansion as “entrainment,” even though the mechanism is rather different from turbulent mixing along the edge of a boundary layer or plume that is typically thought of as entrainment. This is similar to the distinction between “dynamic entrainment” associated with organized inflow and “turbulent entrainment” from smaller-scale mixing that has been discussed in previous papers on cumulus dynamics and convection parameterizations (e.g., de Rooy et al. 2013).

b. Review of analytic theory for thermals

Following dimensional analysis and assuming thermals are self-similar, a set of relationships can be derived to describe thermal behavior² (e.g., [Scorer 1957](#); [Turner 1964](#)). This similarity solution is expressed as

$$B = B_0 \left(\frac{R_0}{R} \right)^3, \quad (4)$$

$$dR/dz = \alpha, \quad (5)$$

$$w^2 = F_r B R, \quad (6)$$

² The self-similar solution is valid when there are no additional length scales, i.e., for flow that is incompressible, neutrally stratified, and in an infinite domain with no buoyancy sources or sinks. Thus, it is expected to break down near boundaries or other discontinuities, when the thermal size approaches a scale height, or when there are additional buoyancy changes, for example, due to phase changes.

where R is the thermal radius, subscript 0 indicates initial values, α is the rate of thermal radius growth with height, and F_r is a Froude number. Note that (6) may be interpreted as a simplified form of the momentum budget given by (3) integrated in time following the thermal. The dimensionless constants α and F_r must be determined empirically, though they can be constrained by invoking the vertical momentum budget (Escudier and Maxworthy 1973) or thermal's impulse-circulation relationship (Turner 1957, 1964; McKim et al. 2020). Following LJ2019 we define a fractional entrainment rate $\epsilon = d(\ln V)/dz$. Combined with (5), this gives $\epsilon = 3\alpha/R$. An entrainment efficiency e can be defined as $e \equiv \epsilon R = 3\alpha$; since α is a constant it follows that e is also a constant.

Integrating (5), combining the resulting expression with (4) and (6), and integrating over time yields (similar to LJ2019)

$$z = at^{1/2} + z_0, \quad (7)$$

where a is a function of α , F_r , and thermal shape [see Scorer (1957) for details] and z_0 is a virtual origin height. Equation (7) is used for our thermal tracking procedure described later.

c. Theoretical estimate of drag coefficient from similarity solution and momentum budget

We combine the thermal vertical momentum equation from section 2a with the similarity solution from section 2b to derive an approximate expression for C_d . First, we express the dynamic and buoyant pressure terms in the momentum budget using the drag law with C_d and a virtual mass coefficient C_v , respectively:

$$F_{pD} = \rho C_d \frac{A}{2V} w^2, \quad (8)$$

$$F_{pB} = \rho(1 - C_v)B, \quad (9)$$

where A is the thermal's horizontal cross-sectional area. The coefficient C_v is defined such that the effective buoyancy—the sum of B and $-F_{pB}/\rho$ —is equal to $C_v B$. For example, $C_v = 2/3$ for a spherical buoyancy perturbation (Tarshish et al. 2018).

Combining (8) and (9) with the momentum budget Eq. (3), multiplying by V/ρ , and rearranging terms gives

$$\frac{d(Vw)}{dt} = C_v B V - \frac{C_d}{2} A w^2, \quad (10)$$

where we have approximated $E \approx -\rho w V^{-1} dV/dt$ in (3) by neglecting the role of entrainment and detrainment driven by small-scale mixing and assuming that entrainment by thermal expansion incorporates environmental fluid with $w = 0$. Using $d/dt = w/dz$ and dividing (10) by Vw^2 gives

$$\frac{d \ln(Vw)}{dz} = \frac{C_v B}{w^2} - \frac{C_d A}{2V}. \quad (11)$$

Following (5) we have $d/dz = \alpha d/dR$, and define a “shape parameter” $\gamma \equiv RA/V$, where γ is a constant following self-

similarity (e.g., $\gamma = 3/4$ for a sphere). Combined with (6), this yields

$$\alpha \frac{d \ln(Vw)}{dR} = \frac{C_v}{F_r^2 R} - \frac{\gamma C_d}{2R}. \quad (12)$$

Finally, we combine (4) and (6) to give $Vw = \beta R^2$, where β is a constant. Substituted into (12), this yields after rearranging terms:

$$C_d = \frac{2}{\gamma} \left(\frac{C_v}{F_r^2} - 2\alpha \right). \quad (13)$$

We emphasize that this derivation does not provide a self-contained solution for C_d since it relies on empirical specification of parameters α , γ , F_r , and C_v , but does constrain C_d provided these parameters are known and the similarity solution is valid. Scorer (1957) found $\alpha = 1/4$ and $F_r^2 = 6/5$. Together with $C_v = 0.57$ from Tarshish et al. (2018) and $\gamma = 3/4$ for spheres, (13) gives $C_d \approx 0.15$. Using parameters from the turbulent thermal simulations of LJ2019 with $F_r^2 \approx 2.5$ and $\alpha \approx 0.15$ gives $C_d \approx -0.09$. Overall, these results suggest a small magnitude of drag and C_d for thermals, at least beyond spinup time when the similarity solution is expected to provide a reasonable approximation of thermal behavior.³ Numerical simulations described in section 4 calculate C_d directly from the dynamic perturbation pressure field and thermal properties. We evaluate the theoretical expression (13) using values of α , γ , C_v , and F_r from the simulations and compare with the directly calculated C_d .

3. Numerical simulations: Model description and setup

a. Model description

This study uses the Cloud Model 1 (CM1; Bryan and Fritsch 2002) to numerically simulate rising dry thermals in a LES configuration based on the filtered Navier–Stokes equations. CM1 is a nonhydrostatic fluid model used primarily for atmospheric flows (both dry and moist). We utilize the incompressible Boussinesq dynamics solver option. Prognostic model variables are the 3D components of flow velocity (u , v , w) and potential temperature perturbation θ' , with pressure retrieved diagnostically. Buoyancy B is obtained by $g\theta'/\theta_0$, where g is a gravitational acceleration constant and θ_0 is a constant background θ of the fluid environment. In this framework prognosing θ' is equivalent to prognosing B itself. Simulations are nondimensionalized based on a length scale equal to the initial thermal radius R_0 (radius of the initial buoyancy perturbation), time scale given by $\sqrt{R_0/B_0}$, where B_0 is the thermal's initial buoyancy, and density scale ρ_0 equal to the background fluid density in the Boussinesq framework

³ Note that our simulations suggest $\gamma \sim 1.25$ and ~ 1 for laminar and turbulent thermals, respectively, as shown in section 4. Using these values leads to a 25%–40% decrease in magnitude of C_d , but does not affect the overall picture of weakly negative to nearly zero C_d .

TABLE 1. Details of the two CM1 configurations used in this study. All quantities are nondimensional; see text for details.

	LOWRES	HIGHRES
Dynamics	Incompressible Boussinesq	Incompressible Boussinesq
Grid length	0.1	0.02
No. of horizontal grid points	320×320	560×560
No. of vertical grid points	640	800
Time step	0.0362	0.00767
Total integration time	65.1	18.4
Advection	Fifth-order WENO	Fifth-order WENO
Subgrid-scale mixing	Smagorinsky type	Smagorinsky type
Lateral boundary conditions	Periodic	Periodic
Lower and upper boundary conditions	Free slip and rigid	Free slip and rigid

(all other quantities are nondimensionalized following these basic scales).

We use two main configurations of CM1. In the first, we use relatively low spatial resolution with horizontal and vertical grid spacings equal to $1/10$ of R_0 (LOWRES). Because the thermals grow rather quickly as they ascend, the overall dynamical structure (e.g., the toroidal circulation) is well resolved with roughly 20–40 grid points horizontally and vertically across the thermal. However, because the dissipation scale (the model’s filter scale) is a relatively large fraction of the thermals’ radii, the resolved-scale flow is smooth and thus appears laminar. In the second set of runs we use higher spatial resolution relative to the thermal size, with the horizontal and vertical grid spacings equal to $1/50$ of R_0 (HIGHRES). In this set of runs the dissipation scale is small relative to the thermal size, and the flow near and within the thermals rapidly (within $t \sim 3$) develops small-scale, turbulent-like eddies, particularly along the upper thermal edge.

In contrast to HIGHRES, turbulent eddies are mostly unresolved in LOWRES and their impact therefore should be mostly represented by the subgrid-scale (SGS) mixing scheme (scheme details given below). However, the impact of SGS mixing in LOWRES differs from the impact of mixing by resolved turbulent eddies (plus SGS mixing) in HIGHRES. This leads to noticeable differences in the thermals’ organized flow between LOWRES and HIGHRES (e.g., the azimuthally averaged flow around the thermals’ central vertical axes) that are detailed in sections 4 and 5. Despite our use of LES with a traditional SGS scheme, the resolved-scale flow in LOWRES is remarkably similar to the direct numerical simulation (DNS) of laminar thermals from LJ2019. Moreover, the turbulent thermals in HIGHRES are very similar to the turbulent thermals in the DNS of LJ2019.

Here we use LES with the filtered Navier–Stokes equations instead of DNS to retain a close connection to atmospheric modeling, particularly future work exploring drag on moist thermals in clouds in which DNS is not possible given the huge $O(10^9)$ Reynolds number. Bryan et al. (2003) showed that an “effective” Reynolds number R_e in LES scales with $(L/\Delta x)^{4/3}$, where L is the length scale of the flow feature and Δx is the model’s grid spacing (see section 3 therein). It follows that there is about an order-of-magnitude difference in R_e between the LOWRES and HIGHRES simulations. This is close to the factor of 10 difference in actual Reynolds

number (using fixed viscosities) between the laminar and turbulent DNS of LJ2019. Given this and the similarities in flow compared to LJ2019 mentioned above, we treat the LOWRES and HIGHRES thermals as analogs of laminar and turbulent thermals. It follows that we will refer to the thermals in LOWRES and HIGHRES as “laminar” and “turbulent,” respectively.

Advection of prognostic variables is calculated using a fifth-order weighted essentially nonoscillatory scheme (WENO; Jiang and Shu 1996). SGS mixing follows a Smagorinsky-type approach as implemented by Stevens et al. (1999, see their appendix B, section b). The mixing length is set to the model grid length. Minimum allowed values of SGS diffusion coefficients for mixing of scalars and momentum are set by applying a minimum nondimensional deformation of 5.5×10^9 for LOWRES and 1.95×10^8 for HIGHRES. There is also a stability-dependent correction that depends on the Richardson number [see Eq. (B13) in Stevens et al. 1999].⁴ Simulations are integrated for nondimensional time of 65.1 for LOWRES. For HIGHRES, we integrate for a time of 18.4 but only analyze simulations before thermal top reaches a nondimensional distance of 2.5 ($2.5 \times R_0$) from the model top. This occurs between $t = 16$ and 17 for the HIGHRES simulations. Other details of the setup are given in Table 1.

Thermals are inserted into the initial conditions by applying $B = 1$ within a sphere of radius $R = 1$ (nondimensional units), with zero buoyancy elsewhere. Thermals are initially centered horizontally within the domain at a height of 8 above the lower boundary for LOWRES and 1.6 for HIGHRES. Additional simulations (not shown) indicate changing the initial height of the thermals or domain size has limited impact on results and does not affect our conclusions. In all simulations, small, gridscale random perturbations are added to the initial buoyancy within the thermal with values between ± 0.1 . To improve robustness, particularly given noise in C_d , we generate ensembles for both LOWRES and HIGHRES by applying different random number seeds for these perturbations. The LOWRES and HIGHRES ensembles consist of eight and five members, respectively.

⁴ Although the background environment is neutrally stable in our setup, local vertical gradients in B can lead to a non-zero Richardson number locally and hence the stability correction may be applied.

For the thermal tracking and all subsequent analysis we use model output in (nondimensional) time increments of 0.55 for LOWRES and 0.15 for HIGHRES. The buoyant and dynamic perturbation pressure fields are diagnosed by solving the corresponding elliptic pressure equations identically to the incompressible solver within CM1. For calculating the thermal's w budget from the simulations,⁵ the tendency term dw/dt is calculated directly from model output using centered finite differencing in time. The buoyant and dynamic pressure forcing terms are calculated directly from the diagnostic p_B and p_D fields using centered differencing in space. Thermal-mean B is obtained directly from model output. The entrainment term E is calculated as a residual, meaning that the sum of the terms on the rhs of (3) is precisely equal to dw/dt .

b. Thermal analysis methodology

Thermal boundaries must first be identified and tracked in order to analyze thermal behavior including drag. To do so we use a method similar to LJ2019, but extended here using an iterative procedure. For each time slice, the horizontal thermal midpoint is determined by the column with maximum vertically integrated pressure perturbation. This is slightly different from LJ2019, who defined the thermal midpoint using w (see their appendix B). At the first step in the iterative process, thermal top is defined by the buoyancy field analogously to LJ2019: the provisional thermal top height z_{top} is calculated as the highest level where the horizontally averaged $B \geq 1/10$ of the maximum horizontally averaged B (maximum defined in the vertical). This is done at each time slice to generate a time series of provisional z_{top} . Model output is then azimuthally averaged around the horizontal midpoint using a radial-vertical grid (r, z) with the same grid spacing as the original Cartesian grid.

As discussed in LJ2019, the thermal volume is rather sensitive to thermal top velocity $w_{\text{top}} \equiv dz_{\text{top}}/dt$. Using the z_{top} obtained directly from the B field as described above can result in considerable noise in w_{top} . Following LJ2019, we instead calculate this derivative by fitting the analytic scaling relation given by (7); that is, the best fit a and z_0 are determined. For determining these parameters, output for $t < 5$ and < 10 are excluded as spinup in HIGHRES and LOWRES, respectively. This difference accounts for somewhat slower spinup of the LOWRES thermals, although applying the fitting for $t > 5$ in the LOWRES has little impact on results including drag. We then take the derivative of (7) analytically to obtain a provisional w_{top} using the fit parameters. From this provisional w_{top} we calculate the Stokes streamfunction using the thermal-relative flow field. This is done by integrating

$$\frac{\partial \psi}{\partial r} = 2\pi r(w_{\text{axi}} - w_{\text{top}}), \quad (14)$$

$$\frac{\partial \psi}{\partial z} = -2\pi r w_{\text{axi}}, \quad (15)$$

⁵ Here we calculate a w budget instead of a momentum (ρw) budget for convenience; these are analogous given ρ is constant in our incompressible Boussinesq framework.

where u_{axi} and w_{axi} are the regridded radial and vertical velocities in cylindrical coordinates, with the boundary condition $\psi(r=0, z=z_{\text{top}}) = 0$. The boundary of the thermal is the $\psi = 0$ contour. In subsequent iteration steps, we use the ψ field from the previous step to calculate a new z_{top} time series based on the maximum height of the $\psi = 0$ contour. The new z_{top} is then used to recalculate w_{top} using the fitting procedure described above. This process is repeated until convergence. Results do not depend on the method for defining provisional z_{top} at the first step; tests show convergence to the same thermal boundaries even when this provisional z_{top} is altered. Thermal total and volume-averaged properties are then calculated using the "final" thermal boundaries obtained from this iterative procedure. R is defined at the level having the widest region with $\psi \geq 0$. Entrainment efficiency e is calculated as the product of the fractional entrainment rate ε and R , with ε calculated from $d(\ln V)/dz_{\text{top}}$ (where V is defined by the volume with $\psi \geq 0$) using centered finite differencing.

Results of the thermal tracking procedure are shown in Fig. 1 for single realizations of the LOWRES and HIGHRES configurations. The thermal w_{top} and z_{top} defined by the buoyancy using the approach of LJ2019 during the first iteration step are shown by red lines in Fig. 1. These z_{top} values are seen to approximately follow the analytic scaling $z_{\text{top}} \propto t^{1/2}$ used in subsequent steps in the iterative thermal tracking procedure. As a basic check, it is seen that w_{top} using the iterative procedure and the thermal volume-averaged w are almost indistinguishable after $t = 10$ (cf. the black and green lines in Figs. 1a,c). The validity of our thermal tracking approach is also supported by closeness of the time series for w_{top} with the w_{top} obtained by directly fitting to $w_{\text{top}} = a_w t^{-1/2}$ (i.e., using best fit a_w); compare the blue and green lines in Fig. 1a. Similarly, the z_{top} obtained from the analytic scaling is very close to z_{top} calculated directly from the streamfunction (Figs. 1b,d).

4. Numerical simulations: Results

a. LOWRES simulations

Figure 2 shows vertical cross sections of thermal boundaries and fields of w , B , p_B , p_D , vorticity in the y - z plane η_y , and contours of streamfunction ψ at three different times from one member of the LOWRES ensemble. The general flow consists of a central region of both thermal-relative and absolute (relative to the fixed model bottom/top boundaries) ascent with descent on the periphery. This flow structure is similar to Hill's analytic spherical vortex, particularly earlier in the simulation. Later in the simulation the thermal flattens owing to thermal expansion and lateral growth from baroclinic vorticity generation (McKim et al. 2020; MPS2021), thereby losing its initially spherical shape and becoming spheroidal. This process leads to an increase in thermal volume as it rises. Environmental fluid entrained by this thermal expansion is quickly wrapped around the toroidal circulation and into the central core. This leads to a rapid reduction of B near the thermal center (Fig. 2a). Buoyancy then becomes concentrated in a ring near the maximum $|\eta_y|$. The p_B field features

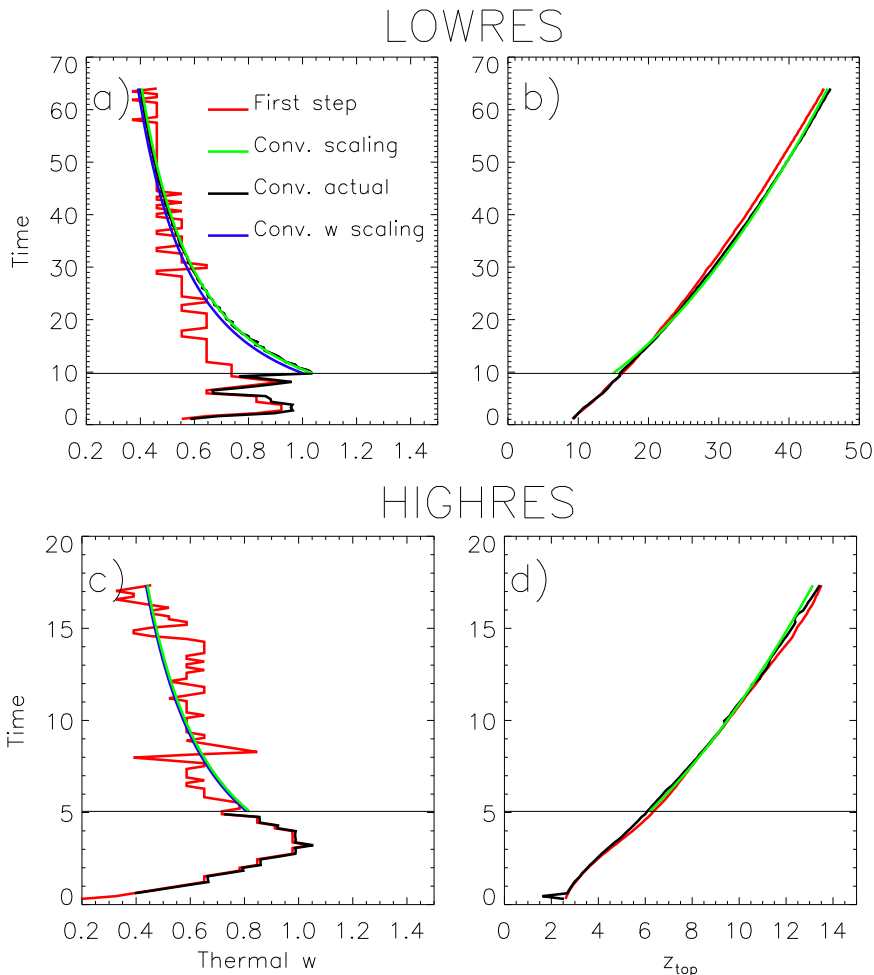


FIG. 1. Time series of (a),(c) thermal vertical velocity w and (b),(d) thermal top height z_{top} . Results are shown for single realizations of the (top) LOWRES and (bottom) HIGHRES. The vertical velocity at thermal top (w_{top}) and z_{top} defined by the buoyancy field on the first iterative step (“first step”) are shown by red lines, the converged w_{top} and z_{top} using the best-fit analytic scaling $z_{\text{top}} = at^{1/2} + z_0$ and iterative method (“conv. scaling”) are shown by green lines, the converged thermal volume-averaged w and z_{top} based on the $\psi = 0$ streamline (“conv. actual”) are shown by black lines, and w_{top} directly fit to $w_{\text{top}} = a_w t^{-1/2}$ (“conv. w scaling”) are shown by the blue lines in (a) and (c). Note that the black lines for thermal volume averaged w are very close to the green lines for $t > 5$ and are therefore not visible in (a) and (c). The horizontal black lines indicate the time beyond which the iterative analytic scaling method is used to track thermal boundaries.

positive values in the upper part of the thermal and negative values in the lower part (Fig. 2b). This leads to a downward-directed net p_B gradient force that partially opposes the thermal’s upward buoyant force. The p_D field has a characteristic high–low–high pattern from thermal top to bottom, with p_D minima associated with the rotational flow coinciding with the $|\eta_y|$ maxima (Figs. 2b,c); see appendix B of Jeevanjee and Romps (2015) for discussion of similar p_D field features.

Behavior of the simulated thermals is also illustrated by time series of thermal radius R , thermal volume-mean w , entrainment efficiency e , and thermal top height z_{top} (Fig. 3). Results are shown for all eight members of the LOWRES

ensemble after $t = 10$ (i.e., excluding spinup). There is ensemble spread in all of the quantities shown in Fig. 3 which reflects perturbations to the initial buoyancy field within the thermals. However, behavior is similar among the ensemble members, and consistent with the analytic similarity solution (see section 2b). Thermal R for all simulations closely follows the theoretical scaling $R \propto z$ which gives $R \propto t^{1/2}$. This is consistent with nearly constant e (and α), though it decreases slightly from $t = 10$ to ~ 30 and is rather noisy for individual simulations. This noise is mainly due simply to noise inherent in calculating derivatives using finite differencing. Taking an average of all ensemble members from $t = 10$ to the end of the

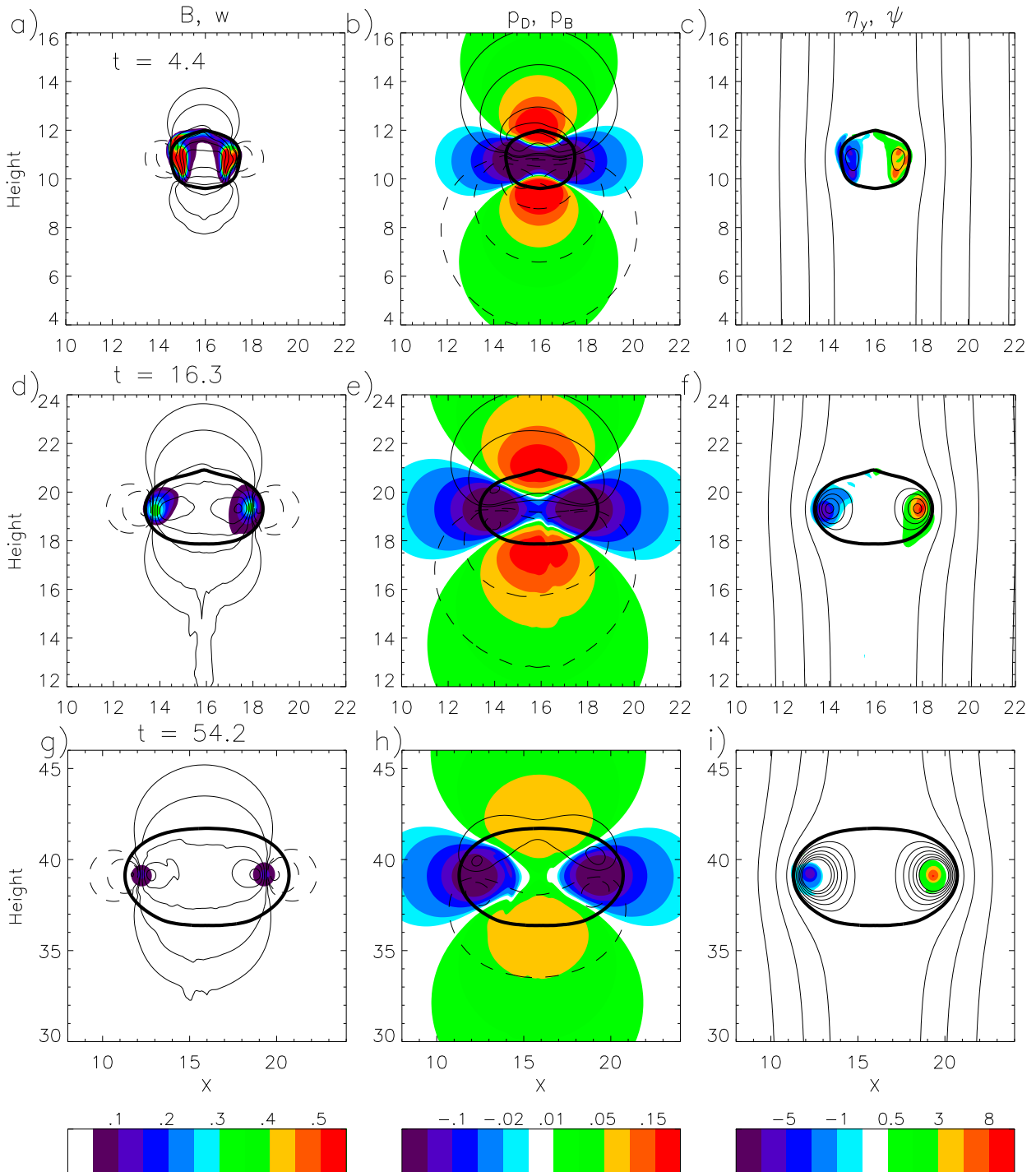


FIG. 2. Vertical cross sections through the domain center from one realization of the LOWRES ensemble at $t =$ (top) 4.4, (middle) 16.3, and (bottom) 54.2. (left) Nondimensional buoyancy B (color contours) and vertical velocity w (thin black solid lines for positive w and thin black dashed lines for negative w , contour values are $\pm 0.1, 0.2, 0.6$, and every 0.4 thereafter). (center) Nondimensional dynamic pressure p_D (color contours) and buoyant pressure p_B (thin black solid lines for positive p_B and thin black dashed lines for negative p_B , contour values are $\pm 0.01, 0.02, 0.06$, and every 0.04 thereafter). (right) Nondimensional horizontal (in y - z plane) vorticity η_y (color contours) and streamlines ψ (thin black contour lines). The thermal boundary corresponding to $\psi = 0$ is shown by the thick black lines in all three panels. Only part of the model domain is shown.

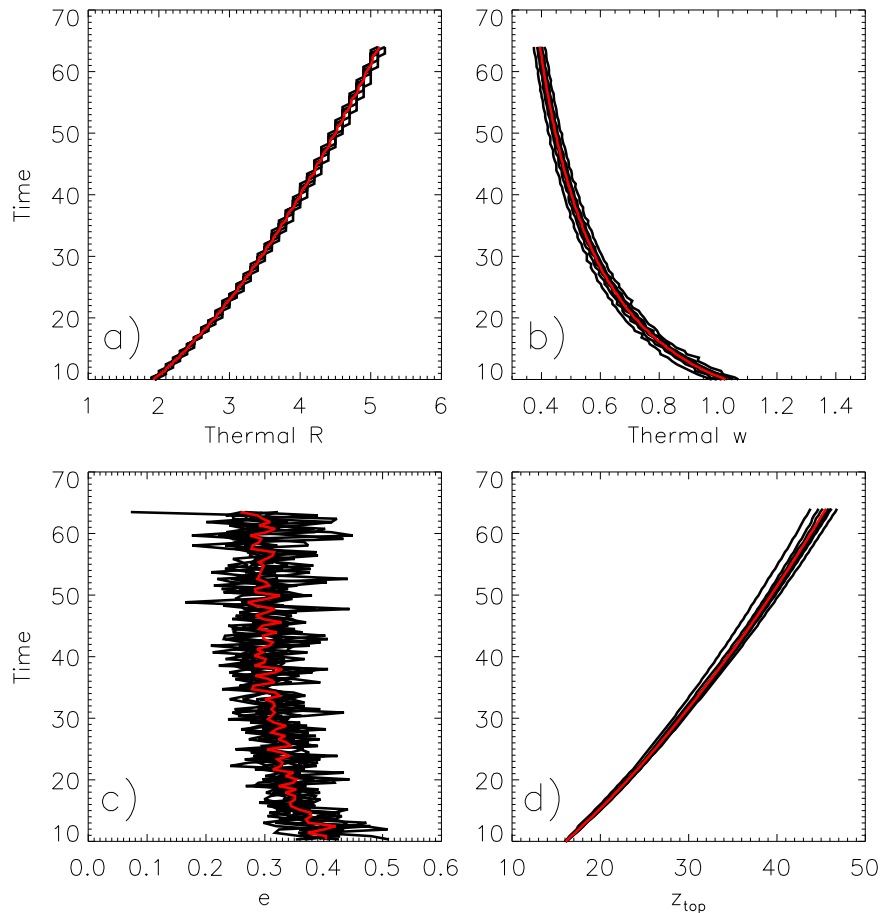


FIG. 3. Time series of (a) thermal radius R , (b) volume-average thermal w , (c) entrainment efficiency e , and (d) thermal-top height z_{top} based on the $\psi = 0$ streamline for the eight members of the LOWRES ensemble. Black lines show individual ensemble members and red lines show the ensemble mean.

integrations gives $e = 0.31$, consistent with the laminar thermals from LJ2019, though slightly smaller (by 14%) than their average e . Here the time- and ensemble-average $\alpha = 0.11$, consistent with our average e since $\alpha \approx e/3$ as explained in section 2b.

Time series of terms in the thermal momentum budget for one realization of the LOWRES ensemble are shown in Fig. 4. While there are small quantitative differences, other ensemble members produce similar results. After spinup, the budget is mainly a balance between upward B forcing and the sink from entrainment and p_B forcing. The p_D forcing is small, consistent with the small dynamic pressure drag discussed later. The sink terms are larger than the source term leading to a decrease of thermal w over time that closely follows the analytic $w \propto t^{-1/2}$ scaling.

The thermals' buoyant forcing follows a general $B \propto t^{-3/2}$ scaling consistent with the similarity solution in section 2b. The p_B forcing term is initially 1/3 the magnitude of the thermals' buoyant forcing consistent with theory for a spherically shaped positive buoyancy anomaly (Tarshish et al. 2018). Its

magnitude decreases after spinup to a value of ~ 0.5 that of the buoyant forcing. This occurs because the initial B field is rapidly distorted by thermal expansion, driving entrainment of nonbuoyant environmental fluid (mainly from underneath the thermal; see also Scorer 1957) followed by the internal transport of this fluid around the thermal's toroidal circulation. This leads to the "flattened ring" of buoyancy as seen in Figs. 2b and 2c (appearing as two lobes of positive buoyancy on the right and left sides of the thermal in vertical cross sections). The p_B forcing scales with the aspect ratio (width to height) of the buoyancy anomaly (e.g., Tarshish et al. 2018), explaining why its magnitude increases relative to the B forcing as the thermal's B field becomes flattened. Consistent with this picture, the virtual mass coefficient C_v decreases from 2/3 (the theoretical value for a buoyant sphere) initially to ~ 0.5 after spinup (Fig. 5a). After $t = 10$, the time- and ensemble-averaged value of this ratio is 0.52. These results are consistent with the theoretical arguments and numerical simulations of Tarshish et al. (2018), who showed a similar decrease of C_v from 2/3 for an initially spherical thermal to ~ 0.57 for the

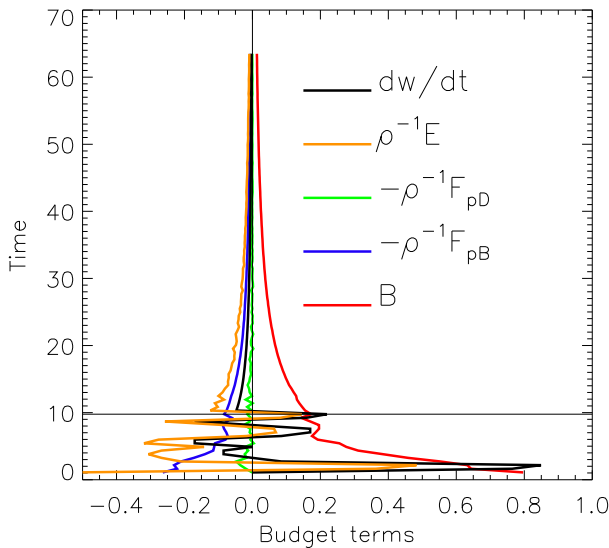


FIG. 4. Time series of terms in the thermal vertical velocity budget for one realization of the LOWRES ensemble. Terms are thermal vertical acceleration dw/dt (black), buoyant forcing B (red), dynamic pressure forcing ($-\rho^{-1}F_{pD}$, green), buoyant pressure forcing ($-\rho^{-1}F_{pB}$, blue), and entrainment calculated as a residual ($\rho^{-1}E$, orange). The horizontal black line indicates the time beyond which the iterative analytic scaling method is used to track thermal boundaries.

mature thermal that was spheroidal. Nearly constant C_v for $t > 10$ here is consistent with a self-similar shape of the thermals and buoyancy fields underpinning the similarity solution outlined in section 2b. Self-similarity of the thermals after spinup is further indicated by time series of shape parameter $\gamma \equiv AR/V$ (Fig. 5b). It is initially close to $3/4$, consistent with a spherical thermal geometry, then increases to a nearly constant value of 1.25 corresponding to the spheroidal thermal shape.

Figure 5c shows time series of Froude number F_r calculated directly from the simulations as $w_{th}/\sqrt{B_{th}R}$. After about $t > 5$, F_r is close to constant in time. The time- ($t \geq 10$) and ensemble-average F_r is 1.51. There is spread among the ensemble members that tends to increase over time.

Overall, the drag coefficient C_d is very small (≈ 0.01) relative to that for a solid sphere or ellipsoid in flow, consistent with the theoretical arguments in section 2c. Figure 5d shows time series of C_d calculated directly as $C_d = 2F_{pD}V/(\rho Aw_{th}^2)$, where the thermal area $A = \pi R^2$ in our axisymmetric analysis framework (see section 3b). For $t < 10$, C_d is noisy with the mean generally between 0.05 and 0.15. Ensemble-mean C_d decreases thereafter to values $\sim 0-0.02$. C_d values for individual simulations after $t = 10$ generally range between -0.05 and 0.05 , indicating the ensemble spread. Applying ensemble and time-averaged values (for $t \geq 10$) of α , γ , C_v , and F_r in the theoretical estimate from (13) gives $C_d \approx 0.02$, close to 0 and consistent with the directly calculated C_d from the simulations of $\sim 0-0.02$.

b. HIGHRES simulations

With the effective Reynolds number of the modeled flow greater by about an order of magnitude compared to the

LOWRES simulations (see section 3a), thermals in the HIGHRES simulations rapidly develop small-scale fluctuations of velocity and B resembling turbulent flow. Vertical cross sections of B , w , p_D , p_B , η_y , ψ , and thermal boundaries are shown in Fig. 6 in the same format as Fig. 2 for the laminar thermals. Three different times are shown: $t = 3.1$, 10.8, and 15.4.

The small-scale fluctuations initially appear near the upper edge of the ascending thermal (Fig. 6a) but later spread through the thermal volume and below in its wake (Figs. 6b,c). However, after spinup the small-scale eddies remain concentrated more in the upper part of the thermals as seen in η_y field, and thus turbulence is vertically asymmetric about the thermal's horizontal central axis. This asymmetry, also seen in the DNS of turbulent thermals in LJ2019, likely occurs because it takes finite time for nonturbulent environmental fluid entrained by thermal expansion, particularly from lateral thermal growth, to develop small-scale eddies as this environmental fluid is wrapped around the toroidal circulation into the central region and then upward by thermal relative $w > 0$ in the core. Crucially, this environmental fluid is entrained primarily from below the thermal, as noted by previous authors (Scorer 1957; Li and Ma 2003). This behavior is similar to the engulfment and wrapping of nonbuoyant environmental fluid around the central core and upward discussed earlier.

The turbulent thermals are also consistent with the similarity theory outlined in section 2b, including time series of R , thermal-average w , and z_{top} (Fig. 7). Overall behavior is similar to the LOWRES thermals. The main difference is that the magnitude of $\alpha \equiv dR/dz$ is greater for the turbulent thermals. This difference is qualitatively consistent with LJ2019, although the difference here in α (about 40%) is larger than that in LJ2019 (about 20%). Note there is much more noise in e for the HIGHRES turbulent thermals than LOWRES thermals, which is not surprising. Otherwise the overall momentum budget and balance of terms in HIGHRES is similar to LOWRES (not shown). The only exception is that the dynamic pressure forcing term is small and positive (upward directed) for HIGHRES rather than nearly zero to slightly negative for LOWRES, which is consistent with the differences in drag discussed below.

Time series of C_v , γ , F_r , and C_d are shown in Fig. 8. The behavior of these parameters is also generally similar to the laminar thermals from the LOWRES ensemble. The virtual mass coefficient C_v decreases from $2/3$ to ~ 0.5 . The mean value ($t \geq 5$) is slightly greater for the turbulent thermals (0.54 compared to 0.52). F_r is also approximately constant with height beyond spinup time. However, F_r is smaller than for the HIGHRES turbulent thermals, about 1.25 versus 1.5 for the laminar thermals. This is consistent with the greater entrainment efficiency of the HIGHRES thermals.

Perhaps the most interesting difference compared to the LOWRES laminar thermals is a weakly negative drag for the HIGHRES turbulent thermals. In HIGHRES, values of C_d are close to 0 near spinup, then decrease to -0.2 to -0.3 from $t \sim 1$ to 10, then settle to about -0.1 for the rest of the simulations (with an ensemble spread from roughly -0.05 to -0.15). This behavior contrasts with $C_d \approx 0.01$ for the LOWRES

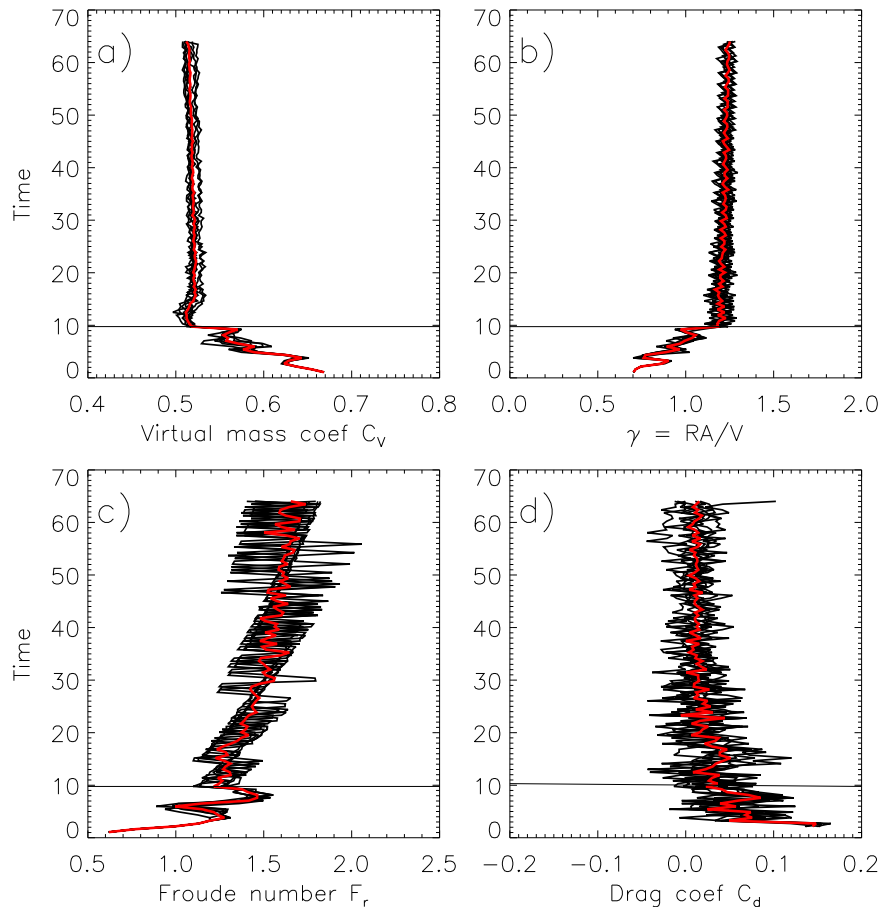


FIG. 5. Time series of (a) virtual mass coefficient C_v , (b) shape parameter γ , (c) Froude number F_r , and (d) drag coefficient C_d from all eight members of the LOWRES ensemble (black lines) and the ensemble mean (red lines). The horizontal black lines indicate the time beyond which the iterative analytic scaling method is used to track thermal boundaries.

thermals. Weakly negative drag for the HIGHRES thermals is robust; all ensemble members at all times for $t > 5$ have negative C_d , and similar C_d values occur using the LJ2019 method to obtain thermal boundaries instead of our iterative method (moreover, the dynamic pressure calculation is calculated by CM1's pressure solver, and thus is internally consistent with the flow calculations in the model). Applying ensemble and time-averaged values (for $t \geq 5$) of α , γ , C_v , and F_r in the theoretical estimate from (13) gives $C_d \approx -0.05$ for the turbulent thermals, close to the actual $C_d \approx -0.1$.

We apply a Welch's t test to examine statistical significance of the differences in C_d between the LOWRES and HIGHRES thermals (valid for unequal sample sizes and variances). We compare time-averaged C_d values ($t \geq 10$, when C_d is fairly steady for both LOWRES and HIGHRES) for the eight-member LOWRES and five-member HIGHRES ensembles. The t statistic is 9.85 (degrees of freedom equal to 4), and the difference in C_d between the two ensembles is statistically significant at a 99.9% confidence level. As we discuss below, weakly negative drag for the HIGHRES thermals and nearly zero drag for LOWRES are also consistent with the respective flow fields.

Weakly negative drag for the HIGHRES thermals may seem counterintuitive, but it is consistent with fundamental physical constraints. From an energetics standpoint, negative drag implies turbulent thermals are more efficient at converting buoyant potential energy into kinetic energy within the thermal (more kinetic energy for the thermal and less for the environment, all else equal), than the LOWRES thermals with nearly zero drag. Thus, negative drag does not violate energy conservation. In other words, since the fluid is initially motionless, kinetic energy everywhere in the domain must come from buoyant potential energy, while drag and entrainment affect how it is partitioned between the thermal and environment. A key is that the thermals are not steady state—most importantly, they entrain mass from the surrounding fluid and expand in volume over time. This implies an effective “entrainment force” that acts in opposition to negative drag (upward-directed force) and buoyant forcing on the thermal, consistent with the momentum budget and d'Alembert's principle. In contrast, negative drag is impossible for a solid body in statistically steady flow since it cannot exchange mass with the surrounding fluid.

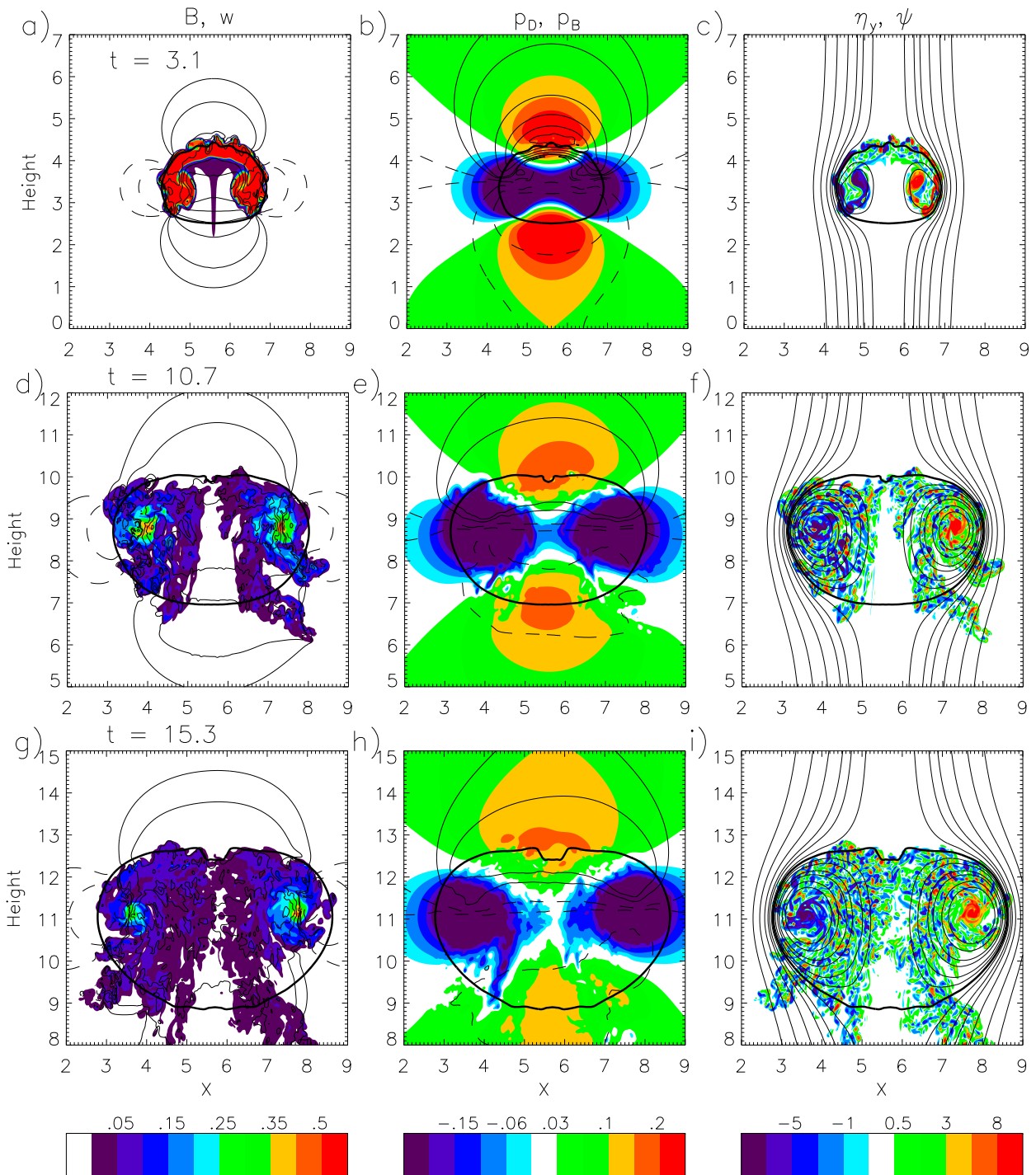


FIG. 6. As in Fig. 2, but for one realization of the HIGHRES ensemble at $t =$ (top) 3.1, (middle) 10.7, and (bottom) 15.3.

c. Interpretation of thermal drag results

Why is drag different for the LOWRES laminar and HIGHRES turbulent thermals? By definition, drag is determined by the volume integral of $-\partial p_D / \partial z$, or alternatively, $p_D \hat{\mathbf{n}} \cdot \hat{\mathbf{k}}$ integrated along the top and bottom thermal surfaces following Gauss's theorem. This means that nonzero drag is associated

with a vertical asymmetry in the p_D field between the top and bottom of the thermal. Vertical asymmetry in p_D in turn *must* fundamentally arise from vertical asymmetry in the flow. This follows from the nature of the Laplacian operator in the Poisson equation for p_D which has the form $\nabla^2 p_D = S$; asymmetric solutions are possible if and only if the "source" term S on the right-hand side, which corresponds to divergence and rotational

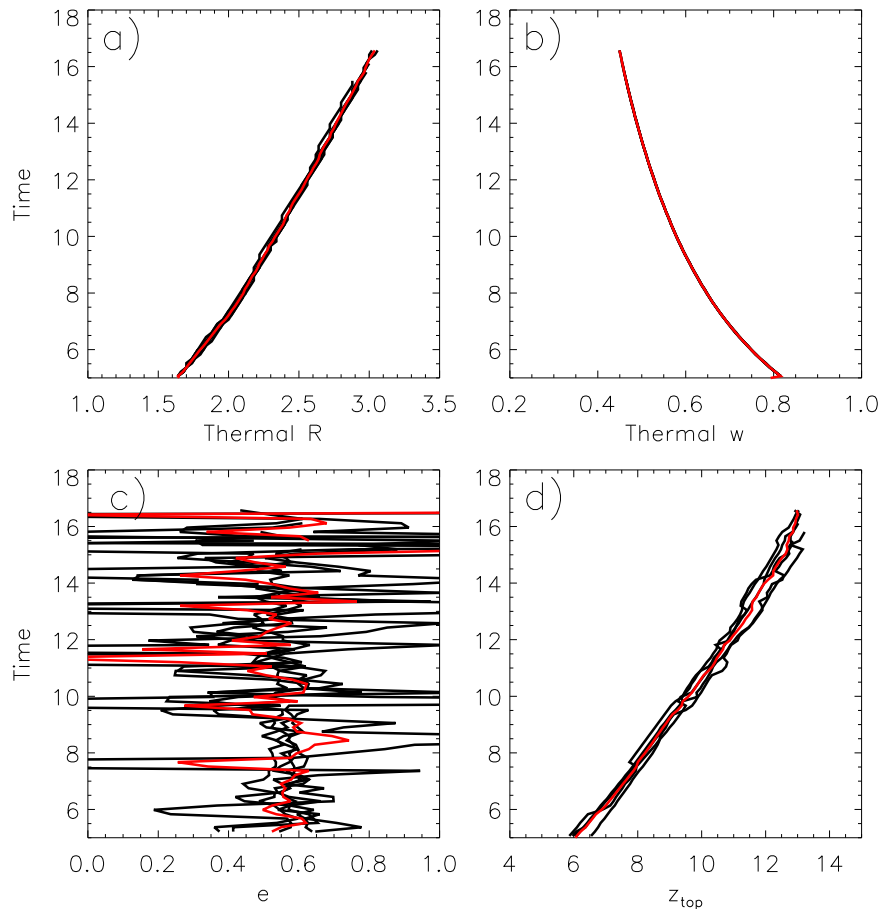


FIG. 7. As in Fig. 3, but for the five-member HIGHRES turbulent thermal ensemble. Note that thermal w for the five different realizations differ but are indistinguishable in the figure.

terms of the flow field, is itself asymmetric (or the boundary conditions are asymmetric, which is not relevant here). Conversely, a vertically symmetric pressure field and hence zero drag must be associated with a vertically symmetric flow field giving a vertically symmetric S in the Poisson p_D equation. A key result is that, after spinup, *thermal-relative flow for the LOWRES laminar thermals is nearly vertically symmetric, whereas it is vertically asymmetric for the HIGHRES turbulent thermals*. Thus, the flow structures of the LOWRES and HIGHRES thermals are consistent with nearly zero drag of the former and nonzero drag of the latter. These flow differences are readily seen from the vertical cross sections in Figs. 2c, 2f, 2i, 6c, 6f, and 6i. For the laminar thermals, the centers of rotation of the azimuthally averaged flow (seen by maxima in ψ and vorticity magnitude, for example, located near $X = 14$ and 19 at a height of 19 in Fig. 2f) are located halfway between the thermal bottom and top, and the streamlines and vorticity fields appear nearly vertically symmetric around this central axis. In contrast, the main centers of rotation for the turbulent thermals are displaced to the upper part of the thermals, about $1/3$ of the distance from the thermal top. For example, the thermal

top is located at a height of 12.6 , the bottom at 8.8 , and the centers of rotation are located near 11.1 – 11.2 for the turbulent thermal in Fig. 6i. These same flow differences were also seen in the DNS of laminar and turbulent thermals in LJ2019, indicating the differences are robust and not due to using a particular model or configuration.

Vertical symmetry of the laminar thermals and asymmetry of the turbulent thermals is further illustrated in Fig. 9. This figure shows vertical profiles of core w (blue lines) and $|\eta_y|$ (red lines), relative to the height of the center of rotation Z_{cen} , at $t \approx 15$. Z_{cen} is defined by the height of maximum ψ . Core w is a horizontal average within $3\Delta x$ of the central vertical axis, while $|\eta_y|$ profiles are a horizontal average across the whole thermal (similar results are obtained for $|\eta_x|$ given axisymmetry of the problem). The laminar thermals are nearly vertically symmetric (Fig. 9a), with only a slight difference (one to two grid points) in distance of Z_{cen} to the top and bottom thermal boundaries and nearly identical profiles of w and $|\eta_y|$ between the upper and lower thermal regions. This symmetry is explained by the structure of the buoyancy field. The thermal's toroidal circulation wraps environmental fluid into its interior and around the circulation centers. As a result,

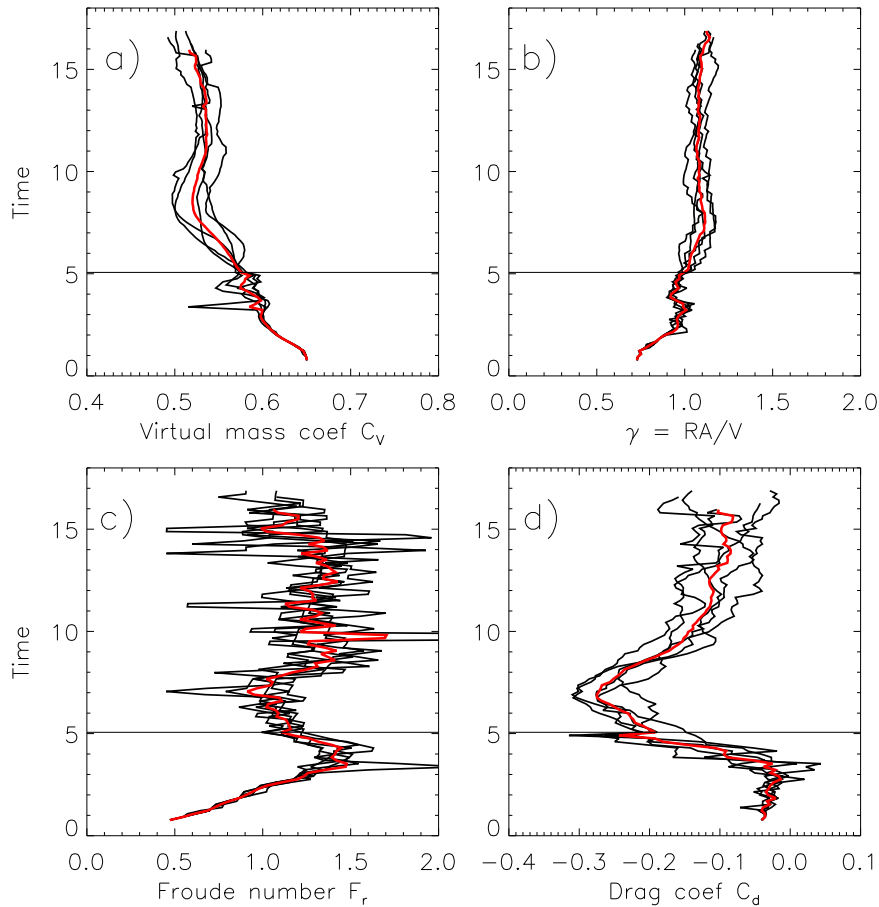


FIG. 8. As in Fig. 5, but for the five-member HIGHRES turbulent thermal ensemble.

nonzero buoyancy quickly becomes concentrated right at these circulation centers and is almost vertically symmetric about them (see Figs. 2b,c). This B structure drives horizontal spread of the thermals (McKim et al. 2020; MPS2021) but they maintain near vertical symmetry. Thus, even though the laminar thermals contain buoyancy and are not steady state, from the standpoint of drag they are very similar to Hill's analytic steady state vortex which formally has no drag (as noted in the introduction, its flow and p_D fields have exact vertically symmetry).

Vertical asymmetry of the flow for the HIGHRES thermals is clearly seen in Fig. 9b. The distance from thermal top to Z_{cen} is much smaller than that from the thermal bottom to Z_{cen} , corresponding to displacement of Z_{cen} to the upper part of the HIGHRES thermals. This is associated with relatively weak w in the upper part of the thermal compared to the lower part as a function of distance from Z_{cen} (cf. the solid and dotted blue lines in Fig. 9b). Note, however, that thermal-relative $w = 0$ both at the top and bottom thermal boundaries, which is indeed required for a coherent rising thermal. Weaker w at a given distance from Z_{cen} in the upper part of the thermal is accompanied by larger $|\eta_y|$. This is consistent with more small-scale velocity fluctuations in that region leading to greater $|\eta_y|$, where these turbulent eddies enhance

dissipation of w momentum associated with the thermal's azimuthally averaged flow compared to lower in the thermal. For example, in Fig. 9 the turbulent thermal shows only a small decrease in $|\eta_y|$ of $\sim 20\%$ from Z_{cen} to the thermal top, while there is a much larger decrease in $|\eta_y|$ between Z_{cen} and the thermal bottom of $\sim 70\%$. This flow structure is associated with a higher thermal-relative, azimuthally averaged flow speed s along the upper compared to lower thermal boundary.⁶ The likely explanation for this asymmetry in turbulence and hence $|\eta_y|$ is because entrainment of environmental fluid occurs near the thermal bottoms and this inflow is mostly laminar since the surrounding environmental flow is mostly laminar (consistent with LJ2019), while it takes time for turbulence to develop as the entrained fluid is wrapped upward into the thermal's core and around its toroidal circulation. This is consistent with less turbulence in the lower part and more turbulence in the upper part of

⁶ Although the flow speed along the thermal's upper boundary is greater than along the lower boundary, total momentum of the azimuthally averaged toroidal circulation flow is much smaller above Z_{cen} than below consistent with overall greater dissipation of the larger-scale flow above Z_{cen} .

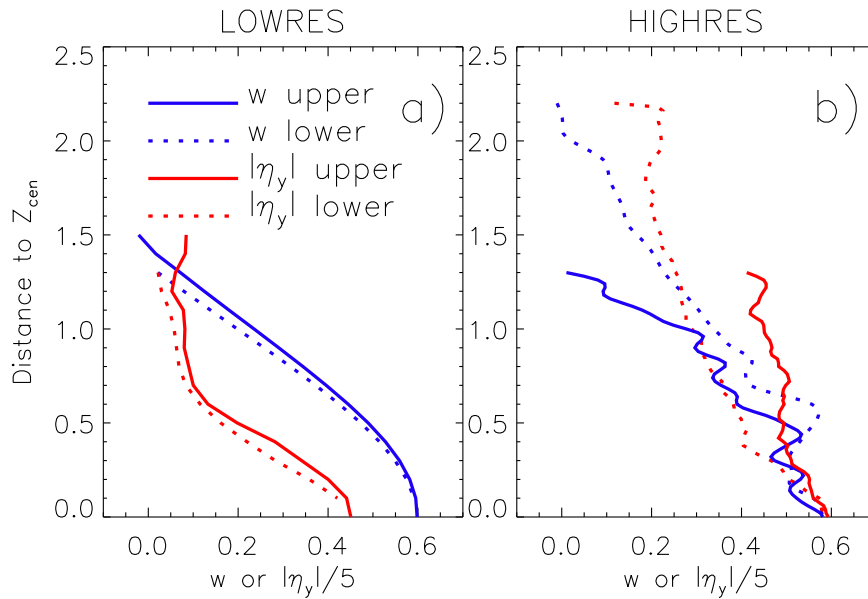


FIG. 9. Vertical profiles of thermal core vertical velocity w (blue lines) and absolute value of vorticity in the y - z plane $|\eta_y|$ (red lines) as a function of distance from thermal's center height Z_{cen} (defined by the height of maximum streamfunction ψ). (a),(b) Results from single realizations of the LOWRES ensemble at $t = 15.2$ and the HIGHRES ensemble at $t = 15.3$. Solid lines show profiles from Z_{cen} to the thermal bottom ("lower") and dotted lines from Z_{cen} to the thermal top ("upper"). Profiles of w are averaged within $3\Delta x$ of the thermal's vertical central axis. Profiles of $|\eta_y|$ are averaged over the whole thermal width.

the thermals (e.g., seen in the η_y field in Fig. 6, especially Figs. 6c and 6f).

Greater flow speed along the upper boundary of the HIGHRES thermals is readily understood by the upward displacement of their rotation centers, meaning streamlines are more tightly packed in the upper part of the thermal. It is also consistent with larger vertical gradients of core w in that part of the thermal (and thus greater horizontal flow speed via mass continuity) consistent with the w profile discussed above. As we noted, vertical asymmetry in the p_D field and hence nonzero drag on the HIGHRES thermals is fundamentally associated with vertical asymmetry of the flow by virtue of the Poisson p_D equation. We can invoke Bernoulli's relation $s^2/2 + p_D/\rho = \text{constant}$ (s is the flow speed) for steady flow along a streamline—in our case, along $\psi = 0$ defining the thermal boundary—to understand qualitatively why faster flow along the upper compared to lower thermal boundary gives negative rather than positive drag (keeping in mind this relation is only approximate, since the thermal's flow is nonsteady and there are contributions from B and p_B , though B is concentrated away from the thermal boundary). At the time shown in Fig. 9, $s^2/2$ is on average 31% higher along the upper compared to lower boundary of the turbulent thermal, consistent with lower p_D along the upper compared to lower boundary. In contrast, the flow speed in LOWRES is almost the same along the lower and upper thermal boundaries (1% higher average $s^2/2$ along the lower compared to upper boundary at the time shown in Fig. 9). A conceptual diagram summarizing results for drag on the LOWRES and HIGHRES thermals is shown in Fig. 10.

Note that the mechanism for how turbulence impacts drag for the HIGHRES thermals is qualitatively different than that for solid bodies in flow. The transition to turbulence at sufficiently high Reynolds number for solid bodies in flow is usually accompanied by a sharp decrease in C_d as a narrow turbulent wake develops (drag crisis). This alters the pressure distribution mainly downstream of the body, leading to a relatively smaller pressure difference on the downstream compared to upstream side of the body and hence reduced C_d compared to laminar flow. In contrast, thermals represent a region within a continuous fluid with a well-defined circulation and exchange of mass with the surrounding fluid, and turbulence in the HIGHRES thermals occurs *within* the thermals, especially in their upper regions. This produces a much different flow and pressure response for thermals and hence impact on drag compared to flows around solid bodies that develop a turbulent wake.

Using mean values of C_D , α , F_r , and γ from the simulations in the theoretical expression (13), we get $C_d \approx 0.02$ for the laminar and ≈ -0.05 for the turbulent thermals. Thus, the theoretical approach—which relies on combining the similarity solution with the w momentum budget—is able to discern between weakly negative drag for the turbulent thermals and very small positive drag for the laminar ones. In the theoretical expression for C_d , this difference in sign arises because of the larger spreading rate α of the turbulent compared to laminar thermals. It is emphasized, however, that correct prediction of the sign of drag by the theory may have been somewhat fortuitous; small C_d from the theory for both the

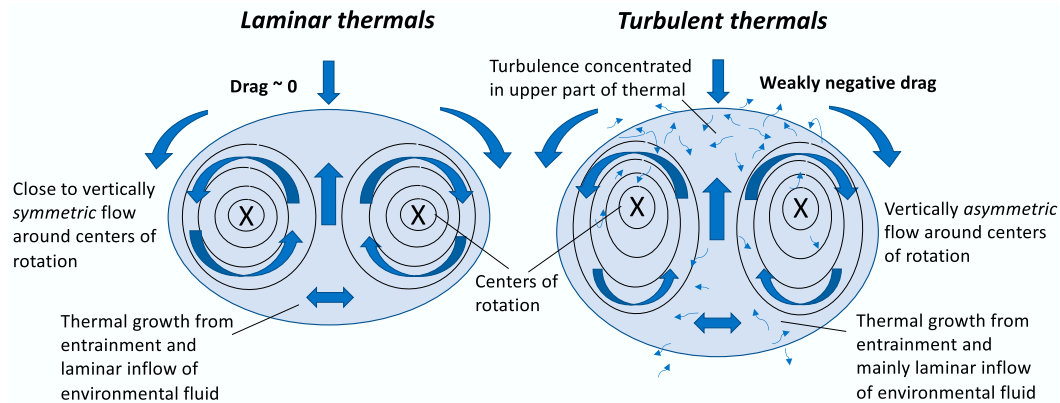


FIG. 10. Conceptual diagram of vertical cross sections showing (left) nearly zero drag for the laminar LOWRES thermals and (right) weakly negative (upward-directed) drag for turbulent HIGHRES thermals. Arrows represent flow and black lines represent streamlines. Flow is nearly vertically symmetric around the centers of rotation (marked with “X”) in the laminar thermals. In the turbulent thermals, turbulence is concentrated in the upper part of the thermals, leading to vertical asymmetry of the flow about the centers of rotation. The centers of rotation are displaced upward which is associated with higher flow speeds and lower pressure along the upper compared to lower thermal boundary, and hence negative drag.

laminar and turbulent cases comes from the difference between order-of-magnitude-larger terms in (13).

5. Summary and conclusions

In this study we investigated dynamic pressure drag on rising dry thermals in a neutrally stable, unsheared environment with incompressible Boussinesq dynamics. Using the drag law $F_d = C_d \rho w^2 A / (2V)$ with F_d equal to the dynamic pressure drag force, a theoretical estimate of C_d was derived based on combining the similarity solution of Scorer (1957) with the thermal momentum budget equation. This estimate gave C_d as a function of four empirically derived parameters: the expansion rate of thermal radius $\alpha \equiv dR/dz$, a parameter γ related to the thermal shape ($\gamma \equiv AR/V$), the virtual mass coefficient C_v , and the Froude number F_r , which are all approximately constant with height for $t > 10$. Using values of these parameters from past studies in this estimate suggests that thermal drag is small, with $C_d \sim -0.1$ to 0.15. This study focused specifically on dynamic pressure drag. There is also an effective “drag” from buoyant pressure forcing on thermals. This forcing can be understood from the shape of the buoyancy field, and our results for buoyant pressure forcing were in line with previous studies (e.g., Tarshish et al. 2018). Namely, the buoyant forcing was reduced by a factor of 1/3 for initially spherical thermals to $\sim 1/2$ after spinup when the thermals became spheroidal and horizontally elongated.

Two sets of numerical simulations of thermals using the CM1 model in LES configuration were analyzed. The first set had a relatively low effective Reynolds number with 20 model grid points across the initial thermals (LOWRES). The second set had about an order-of-magnitude-higher effective Reynolds number with 100 grid points across the initial thermals (HIGHRES). To improve robustness we ran eight and five ensemble members for LOWRES and HIGHRES,

respectively. Both the LOWRES and HIGHRES simulations produced thermals that conformed well to the similarity theory, with approximately constant α , γ , C_v , and F_r after the initial spinup. One notable difference between the LOWRES laminar and HIGHRES turbulent thermals was a 40% higher α for the turbulent thermals, which is consistent with previous results based on DNS of laminar and turbulent thermals (LJ2019). Dynamic pressure drag was small in both the LOWRES and HIGHRES simulations (compared to that for flow around a solid sphere). Thus, the thermal momentum budget was primarily a balance between positive forcing from buoyancy and negative forcing from buoyant pressure forcing and momentum entrainment. Dynamic pressure forcing was an order of smaller magnitude than these other terms.

A key result from this study was a small but robust difference in C_d between the LOWRES laminar and HIGHRES turbulent thermals. After spinup the laminar thermals had $C_d \approx 0.01$, while the turbulent thermals had weakly negative drag with $C_d \approx -0.1$. This difference was explained by near vertical symmetry of the thermal flow in LOWRES but considerable vertical asymmetry in HIGHRES. The difference in drag is simple to understand given that dynamic pressure drag can be defined by the difference in p_D between thermals’ top and bottom boundaries, and asymmetry in p_D requires an asymmetry in the flow. The laminar LOWRES thermals were nearly vertically symmetric because the buoyancy field quickly became concentrated near the centers of rotation of the main toroidal circulation and were nearly symmetric about them. This buoyancy structure led to baroclinic generation of vorticity and thermal expansion (McKim et al. 2020; MPS2021), but this did little to break vertical symmetry of the thermal flow structure.

In contrast, even though buoyancy was also concentrated near the main rotation centers (though somewhat more diffuse than in the laminar thermals), a vertical asymmetry in the

flow occurred for the turbulent HIGHRES thermals. Vertical asymmetry in the azimuthally averaged flow was evident by an upward shift of the main centers of rotation such that they were located about 1/3 of the distance from the thermal top (a result also seen in the turbulent thermal DNS of LJ2019). This shift was mainly attributed to the impact of small-scale eddies concentrated more in the upper part of the thermals, particularly just after spinup when C_d was most negative (~ -0.3). Using values of α , γ , C_b , and F_r obtained directly from the simulations in the theoretical estimate of C_d gave a small magnitude of drag for the simulated thermals. The theoretical estimate was able to discern between very small positive drag for the laminar thermals and weakly negative drag for the turbulent thermals, but this may have been somewhat fortuitous given that small drag in both cases resulted from the difference between order-of-magnitude-larger terms in the theoretical expression. We attributed vertical asymmetry of the azimuthally averaged flow within the turbulent thermals primarily to asymmetry in turbulence, also seen in the DNS of LJ2019. However, we cannot rule out that buoyancy differences during spinup compared to LOWRES (e.g., sharper buoyancy gradients initially in HIGHRES) may have also contributed to vertical asymmetry of the flow even after spinup, in contrast to the flow symmetry in LOWRES.

Given the evident impact of small-scale resolved eddies in HIGHRES, it is plausible that further increases in effective Reynolds number R_e could impact drag on simulated turbulent thermals. For instance, we speculate that small-scale eddies in this case could develop faster in the (thermal-relative) ascending flow of entrained and initially nonturbulent fluid flow in the lower part of the thermal. Faster development of turbulence in this entrained fluid could plausibly reduce the vertical asymmetry in small-scale eddies and thus reduce the magnitude of negative drag. Runs with higher R_e are beyond current computational capability but would be interesting to pursue in future work.

In this study, we focused on the simple case of dry thermals in a neutrally stable, unstratified, unshered environment. As noted in the introduction, recent attention has focused on the properties of moist thermals within cumulus clouds. Latent heating was shown to have a large impact on the structure and dynamics of moist thermals by modifying their buoyancy structure and expansion rate, with a secondary impact of latent cooling from evaporation (MPS2021). It is reasonable to speculate that dynamic pressure drag on moist thermals could also be strongly influenced by phase changes impacting the buoyancy structure. Specifically, a vertical asymmetry in latent heating and hence the B field (see Figs. 2 and 4 in MPS2021) might be expected to drive vertical asymmetry in the flow and thus dynamic pressure drag. Whether latent heating increases or decreases with height (concentrating buoyancy in the upper or lower parts of moist thermals) will depend on the thermodynamic sounding and nature of dilution by entrained environmental air. Moreover, density stratification leads to an increase in the expansion rate of thermals (Anders et al. 2019; MPS2021) and could also drive vertical asymmetry of the flow and hence drag on atmospheric thermals.

Dynamic pressure drag on moist thermals in a stratified environment will be a subject of future work.

There are many other factors that could potentially impact drag on atmospheric thermals that were not considered here. Given the evident impact of vertical asymmetry in small-scale eddies concentrated in the upper part of thermals on the azimuthally averaged flow and drag, it is reasonable to believe that entrainment of air from a turbulent as opposed to laminar environment could impact drag. In particular, this might be relevant to thermals rising within a turbulent PBL versus those rising through a nonturbulent (or weakly turbulent) free troposphere. Finally, there may be sensitivity to the initial thermal shape. Here the thermals were initially spherical. Previous studies (Bond and Johari 2010; Lai et al. 2015) have shown sensitivity of thermal dynamics to the initial shape even after spinup, particularly thermal spreading rates, and it is plausible that nonspherical initial shape could also influence drag after spinup. These topics are beyond the scope of this paper but could be explored in future work.

Acknowledgments. HM was supported by the U.S. Department of Energy Atmospheric System Research Grant DE-SC0020104. The National Center for Atmospheric Research is sponsored by the National Science Foundation. We acknowledge high-performance computing support from Cheyenne (doi:10.5065/D6RX99HX) provided by NCAR's Computational and Information Systems Laboratory. Comments on an earlier version of the paper by Dr. Richard Rotunno are appreciated. We also thank Dr. George Bryan for developing and maintaining CM1. We also thank two anonymous reviewers and Prof. Steven Sherwood for constructive comments and suggestions that improved the paper.

Data availability statement. This study used CM1 version 20.1 (cm1r20.1) released on 25 August 2020. CM1 code and detailed documentation are available at <https://www2.mmm.ucar.edu/people/bryan/cm1/>. Configuration and namelist files for the CM1 simulations as well as analysis code can be made available upon request to the first author.

REFERENCES

- Anders, E. H., D. Lecoanet, and B. P. Brown, 2019: Entropy rain: Dilution and compression of thermals in stratified domains. *Astrophys. J.*, **884**, 65, <https://doi.org/10.3847/1538-4357/ab3644>.
- Blyth, A. M., S. G. Lasher-Trapp, and W. A. Cooper, 2005: A study of thermals in cumulus clouds. *Quart. J. Roy. Meteor. Soc.*, **131**, 1171–1190, <https://doi.org/10.1256/qj.03.180>.
- Bond, D., and H. Johari, 2005: Effects of initial geometry on the development of thermals. *Exp. Fluids*, **39**, 591–601, <https://doi.org/10.1007/s00348-005-0997-1>.
- , and —, 2010: Impact of buoyancy on vortex ring development in the near field. *Exp. Fluids*, **48**, 737–745, <https://doi.org/10.1007/s00348-009-0761-z>.
- Bretherton, C. S., J. R. McCaa, and H. Grenier, 2004: A new parameterization for shallow cumulus convection and its application to marine subtropical cloud-topped boundary layers. Part I: Description and 1D results. *Mon. Wea. Rev.*,

- 132, 864–882, [https://doi.org/10.1175/1520-0493\(2004\)132<0864:ANPFC>2.0.CO;2](https://doi.org/10.1175/1520-0493(2004)132<0864:ANPFC>2.0.CO;2).
- Bryan, G. H., and J. Fritsch, 2002: A benchmark simulation for moist nonhydrostatic numerical models. *Mon. Wea. Rev.*, **130**, 2917–2928, [https://doi.org/10.1175/1520-0493\(2002\)130<2917:ABSFMN>2.0.CO;2](https://doi.org/10.1175/1520-0493(2002)130<2917:ABSFMN>2.0.CO;2).
- , J. C. Wyngaard, and J. M. Fritsch, 2003: Resolution requirements for the simulation of deep moist convection. *Mon. Wea. Rev.*, **131**, 2394–2416, [https://doi.org/10.1175/1520-0493\(2003\)131<2394:RRFTSO>2.0.CO;2](https://doi.org/10.1175/1520-0493(2003)131<2394:RRFTSO>2.0.CO;2).
- Damiani, R., G. Vali, and S. Haimov, 2006: The structure of thermals in cumulus from airborne dual-Doppler radar observations. *J. Atmos. Sci.*, **63**, 1432–1450, <https://doi.org/10.1175/JAS3701.1>.
- Davies-Jones, R., 2003: An expression for effective buoyancy in surroundings with horizontal density gradients. *J. Atmos. Sci.*, **60**, 2922–2925, [https://doi.org/10.1175/1520-0469\(2003\)060<2922:AEFEBI>2.0.CO;2](https://doi.org/10.1175/1520-0469(2003)060<2922:AEFEBI>2.0.CO;2).
- de Rooy, W. C., and Coauthors, 2013: Entrainment and detrainment in cumulus convection: An overview. *Quart. J. Roy. Meteor. Soc.*, **139**, 1–19, <https://doi.org/10.1002/qj.1959>.
- Donner, L. J., 1993: A cumulus parameterization including mass fluxes, vertical momentum dynamics, and mesoscale effects. *J. Atmos. Sci.*, **50**, 889–906, [https://doi.org/10.1175/1520-0469\(1993\)050<0889:ACPIMF>2.0.CO;2](https://doi.org/10.1175/1520-0469(1993)050<0889:ACPIMF>2.0.CO;2).
- Escudier, M. P., and T. Maxworthy, 1973: On the motion of turbulent thermals. *J. Fluid Mech.*, **61**, 541–552, <https://doi.org/10.1017/S0022112073000856>.
- Gan, L., J. R. Dawson, and T. B. Nickels, 2012: On the drag of turbulent vortex rings. *J. Fluid Mech.*, **709**, 85–105, <https://doi.org/10.1017/jfm.2012.322>.
- Hernandez-Deckers, D., and S. C. Sherwood, 2016: A numerical investigation of cumulus thermals. *J. Atmos. Sci.*, **73**, 4117–4136, <https://doi.org/10.1175/JAS-D-15-0385.1>.
- , and —, 2018: On the role of entrainment in the fate of cumulus thermals. *J. Atmos. Sci.*, **75**, 3911–3924, <https://doi.org/10.1175/JAS-D-18-0077.1>.
- Heus, T., H. J. J. Jonker, H. E. A. Van den Akker, E. J. Griffith, M. Koutek, and F. H. Post, 2009: A statistical approach to the life cycle analysis of cumulus clouds selected in a virtual reality environment. *J. Geophys. Res.*, **114**, D06208, <https://doi.org/10.1029/2008JD010917>.
- Jeevanjee, N., 2017: Vertical velocity in the gray zone. *J. Adv. Model. Earth Syst.*, **9**, 2304–2316, <https://doi.org/10.1002/2017MS001059>.
- , and D. M. Romps, 2015: Effective buoyancy, inertial pressure, and the mechanical generation of boundary layer mass flux by cold pools. *J. Atmos. Sci.*, **72**, 3199–3213, <https://doi.org/10.1175/JAS-D-14-0349.1>.
- , and —, 2016: Effective buoyancy at the surface and aloft. *Quart. J. Roy. Meteor. Soc.*, **142**, 811–820, <https://doi.org/10.1002/qj.2683>.
- Jiang, G. S., and C. W. Shu, 1996: Efficient implementation of weighted ENO schemes. *J. Comput. Phys.*, **126**, 202–228, <https://doi.org/10.1006/jcph.1996.0130>.
- Johari, H., 1992: Mixing in thermals with and without buoyancy reversal. *J. Atmos. Sci.*, **49**, 1412–1426, [https://doi.org/10.1175/1520-0469\(1992\)049<1412:MITWAW>2.0.CO;2](https://doi.org/10.1175/1520-0469(1992)049<1412:MITWAW>2.0.CO;2).
- Lai, A. C. H., B. Zhao, A. W.-K. Law, and E. E. Adams, 2015: A numerical and analytical study of the effect of aspect ratio on the behavior of a round thermal. *Environ. Fluid Mech.*, **15**, 85–108, <https://doi.org/10.1007/s10652-014-9362-3>.
- Lecoanet, D., and N. Jeevanjee, 2019: Entrainment in resolved, dry thermals. *J. Atmos. Sci.*, **76**, 3785–3801, <https://doi.org/10.1175/JAS-D-18-0320.1>.
- Li, C. W., and F. Zhang, 1996: Three-dimensional simulation of thermals using a split-operator scheme. *Int. J. Numer. Methods Heat Fluid Flow*, **6**, 25–35, <https://doi.org/10.1108/09615539610113073>.
- , and F. X. Ma, 2003: Large eddy simulation of diffusion of a buoyancy source in ambient water. *Appl. Math. Modell.*, **27**, 649–663, [https://doi.org/10.1016/S0307-904X\(03\)00073-8](https://doi.org/10.1016/S0307-904X(03)00073-8).
- Lilly, D. K., 1962: On the numerical simulation of buoyant convection. *Tellus*, **14**, 148–172, <https://doi.org/10.1111/j.2153-3490.1962.tb00128.x>.
- Lundgren, T. S., J. Yao, and N. N. Mansour, 1992: Microburst modelling and scaling. *J. Fluid Mech.*, **239**, 461–488, <https://doi.org/10.1017/S002211209200449X>.
- Ma, F. X., and C. W. Li, 2001: 3D numerical simulation of ambient discharge of buoyant water. *Appl. Math. Model.*, **25**, 375–384, [https://doi.org/10.1016/S0307-904X\(00\)00061-5](https://doi.org/10.1016/S0307-904X(00)00061-5).
- Markowski, P., and Y. Richardson, 2011: *Mesoscale Meteorology in Midlatitudes*. John Wiley and Sons, 430 pp.
- Maxworthy, T., 1974: Turbulent vortex rings. *J. Fluid Mech.*, **64**, 227–240, <https://doi.org/10.1017/S0022112074002370>.
- McKim, B., N. Jeevanjee, and D. Lecoanet, 2020: Buoyancy-driven entrainment in dry thermals. *Quart. J. Roy. Meteor. Soc.*, **146**, 415–425, <https://doi.org/10.1002/qj.3683>.
- Morrison, H., 2016: Impacts of updraft size and dimensionality on the perturbation pressure and vertical velocity in cumulus convection. Part I: Simple, generalized analytic solutions. *J. Atmos. Sci.*, **73**, 1441–1454, <https://doi.org/10.1175/JAS-D-15-0041.1>.
- , and J. M. Peters, 2018: Theoretical expressions for the ascent rate of moist deep convective thermals. *J. Atmos. Sci.*, **75**, 1699–1719, <https://doi.org/10.1175/JAS-D-17-0295.1>.
- , —, and S. C. Sherwood, 2021: Comparing growth rates of simulated moist and dry convective thermals. *J. Atmos. Sci.*, **78**, 797–816, <https://doi.org/10.1175/JAS-D-20-0166.1>.
- Ogura, Y., 1962: Convection of isolated masses of a buoyant fluid: A numerical calculation. *J. Atmos. Sci.*, **19**, 492–502, [https://doi.org/10.1175/1520-0469\(1962\)019<0492:COIMOA>2.0.CO;2](https://doi.org/10.1175/1520-0469(1962)019<0492:COIMOA>2.0.CO;2).
- Pauluis, O., and S. Garner, 2006: Sensitivity of radiative convective equilibrium simulations to horizontal resolution. *J. Atmos. Sci.*, **63**, 1910–1923, <https://doi.org/10.1175/JAS3705.1>.
- Peters, J. M., 2016: The impact of effective buoyancy and dynamic pressure forcing on vertical velocities within two-dimensional updrafts. *J. Atmos. Sci.*, **73**, 4531–4551, <https://doi.org/10.1175/JAS-D-16-0016.1>.
- Richards, J. M., 1961: Experiments on the penetration of an interface by buoyant thermals. *J. Fluid Mech.*, **11**, 369–384, <https://doi.org/10.1017/S0022112061000585>.
- Romps, D. M., and A. B. Charn, 2015: Sticky thermals: Evidence for a dominant balance between buoyancy and drag in cloud updrafts. *J. Atmos. Sci.*, **72**, 2890–2901, <https://doi.org/10.1175/JAS-D-15-0042.1>.
- , and R. Öktem, 2015: Stereo photogrammetry reveals substantial drag on cloud thermals. *Geophys. Res. Lett.*, **42**, 5051–5057, <https://doi.org/10.1002/2015GL064009>.
- Sánchez, O., D. J. Raymond, L. Libersky, and A. G. Petschek, 1989: The development of thermals from rest. *J. Atmos. Sci.*, **46**, 2280–2292, [https://doi.org/10.1175/1520-0469\(1989\)046<2280:TDOTFR>2.0.CO;2](https://doi.org/10.1175/1520-0469(1989)046<2280:TDOTFR>2.0.CO;2).

- Scorer, R. S., 1957: Experiments on convection of isolated masses of buoyant fluid. *J. Fluid Mech.*, **2**, 583–594, <https://doi.org/10.1017/S0022112057000397>.
- Sherwood, S. C., D. Hernández-Deckers, M. Colin, and F. Robinson, 2013: Slippery thermals and the cumulus entrainment paradox. *J. Atmos. Sci.*, **70**, 2426–2442, <https://doi.org/10.1175/JAS-D-12-0220.1>.
- Siebesma, A. P., and Coauthors, 2003: A large eddy simulation intercomparison study of shallow cumulus convection. *J. Atmos. Sci.*, **60**, 1201–1219, [https://doi.org/10.1175/1520-0469\(2003\)60<1201:ALESIS>2.0.CO;2](https://doi.org/10.1175/1520-0469(2003)60<1201:ALESIS>2.0.CO;2).
- Stevens, B., C. H. Moeng, and P. P. Sullivan, 1999: Large-eddy simulations of radiatively driven convection: Sensitivities to the representation of small scales. *J. Atmos. Sci.*, **56**, 3963–3984, [https://doi.org/10.1175/1520-0469\(1999\)056<3963:LESORD>2.0.CO;2](https://doi.org/10.1175/1520-0469(1999)056<3963:LESORD>2.0.CO;2).
- Tarshish, N., N. Jeevanjee, and D. Lecoanet, 2018: Buoyant motion of a turbulent thermal. *J. Atmos. Sci.*, **75**, 3233–3244, <https://doi.org/10.1175/JAS-D-17-0371.1>.
- Turner, J. S., 1957: Buoyant vortex rings. *Proc. Roy. Soc. London*, **239**, 61–75, <https://doi.org/10.1098/rspa.1957.0022>.
- , 1964: The dynamics of spheroidal masses of buoyant fluid. *J. Fluid Mech.*, **19**, 481–490, <https://doi.org/10.1017/S0022112064000854>.
- , 1973: *Buoyancy Effects in Fluids*. Cambridge University Press, 412 pp.
- Vasel-Be-Hagh, A., R. Carriveau, D. S. Ting, and J. S. Turner, 2015: Drag of buoyant vortex rings. *Phys. Rev. E*, **92**, 043024, <https://doi.org/10.1103/PhysRevE.92.043024>.
- Vybhav, G. R., and S. Ravichandran, 2022: Entrainment in dry and moist thermals. *Phys. Rev. Fluids*, **7**, 050501, <https://doi.org/10.1103/PhysRevFluids.7.050501>.
- Weisman, M. L., W. C. Skamarock, and J. B. Klemp, 1997: The resolution dependence of explicitly modeled convective systems. *Mon. Wea. Rev.*, **125**, 527–548, [https://doi.org/10.1175/1520-0493\(1997\)125<0527:TRDOEM>2.0.CO;2](https://doi.org/10.1175/1520-0493(1997)125<0527:TRDOEM>2.0.CO;2).
- Woodward, B., 1959: The motion in and around isolated thermals. *Quart. J. Roy. Meteor. Soc.*, **85**, 144–151, <https://doi.org/10.1002/qj.49708536407>.
- Yano, J. I., 2014: Basic convective element: Bubble or plume? A historical review. *Atmos. Chem. Phys.*, **14**, 7019–7030, <https://doi.org/10.5194/acp-14-7019-2014>.
- Zhao, B., A. W. Law, A. C. Lai, and E. E. Adams, 2013: On the internal vorticity and density structures of miscible thermals. *J. Fluid Mech.*, **722**, R5, <https://doi.org/10.1017/jfm.2013.158>.
- Zhao, M., and P. H. Austin, 2005: Life cycle of numerically simulated shallow cumulus clouds. Part II: Mixing dynamics. *J. Atmos. Sci.*, **62**, 1291–1310, <https://doi.org/10.1175/JAS3415.1>.